



c-PCBSD, a cross-linked fullerene derivative, as a cathodic interlayer in wide-band gap perovskite solar cells

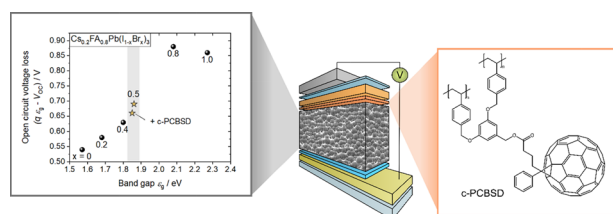
Katarina Gugujonović¹ · Felix Mayr¹ · Bekele Hailegnaw² · Stefan Pöllner¹ · Rene Zahrhuber¹ · Alexander Planer¹ · Chuan-Hsin Wang³ · Chain-Shu Hsu³ · Markus Clark Scharber¹

Received: 23 January 2023 / Accepted: 2 July 2023
© The Author(s) 2023

Abstract

Wide-band gap absorber materials are prerequisites for well-performing tandem photovoltaic devices. Especially, perovskites received huge attention due to their tunable band gap and outstanding optoelectronic properties. Although perovskite solar cells are known to be highly efficient, high-open-circuit voltage losses remain a prevalent issue for wide-band gap perovskites. Within this work, we have investigated the application of the cross-linkable fullerene derivative [6,6]-phenyl-C61-butyric styryl dendron ester (c-PCBSD) as a cathodic interlayer in wide-band gap perovskite solar cells. We could obtain increased open-circuit voltage compared to pristine devices, attributed to fast electron transfer between the perovskite and the interlayer. The changed charge carrier dynamics result in a reduction of non-radiative losses, which consequently decreases the open-circuit voltage loss.

Graphical abstract



Keywords Solar energy · Photovoltaics · Absorption spectra · Charge transfer · Fluorescence spectroscopy

Introduction

Organic–inorganic halide perovskites (OIHPs) have attracted massive attention during the last decade since they are up-and-coming candidates for many novel optoelectronic devices. With their outstanding properties, like long carrier diffusion length [1, 2], high charge mobility [3], and

high absorption coefficient in the visible range of light [3, 4], they are an excellent choice for absorber materials in solar cells. Since their debut in 2009, their power conversion efficiency of single-junction OIHP-based solar cells has remarkably increased from 3.8% [5] to 25.7% [6], which is almost as high as the record for the commercially well-established crystalline silicon solar cells (26.1%, [6]). The efficiency obtained from both photovoltaic technologies is already close to the highest possible value for single-junction solar cells. Shockley and Queisser first determined this limit (SQ limit) in 1961 and calculated a value of around 30% [7]. Multiple absorber layers can enhance the overall device efficiency and allow to surpass the SQ limit. Typically, for double-junction solar cells, a combination of a high- and a low-band gap absorber is required. A prevalent

✉ Katarina Gugujonović
katarina.gugujonovic@jku.at

¹ Institute of Physical Chemistry, Johannes Kepler University, Linz, Austria

² Division of Soft Matter Physics, Institute of Experimental Physics, Johannes Kepler University, Linz, Austria

³ Department of Applied Chemistry, Center of Emergent Functional Matter Science, Hsinchu, Taiwan

variety is silicon with an OIHP. Since perovskites have the possibility of band gap tuning, which can be conducted by simply changing the composition of the perovskite crystal [8], their band gap can be easily adjusted to match with the low band gap of silicon (1.12 eV [9]). The ideal band gap of the perovskite sub-cell in a silicon–perovskite (series-connected) tandem configuration is 1.67–1.75 eV [10]. The current efficiency record for a silicon–perovskite tandem solar cell is 32.5% [11]. Another promising approach is the combination of an organic and a perovskite solar cell into a tandem cell. With the current development of novel non-fullerene acceptors, materials with a spectral response up to 1130 nm are available [12]. For a low band gap range of 1.1–1.25 eV, a perovskite wide-band gap absorber with a band gap of 1.69–1.87 eV would be required for optimum band gap matching [13]. This range can be achieved with OIHP compositions of $\text{Cs}_{0.2}\text{FA}_{0.8}\text{Pb}(\text{I}_{1-x}\text{Br}_x)_3$ by varying the bromide content x from 0.2 to 0.5. For instance, in a tandem device with IEICO-4F:PTB7-Th as low-band gap absorber, a perovskite sub-cell with an optical band gap of > 1.82 eV is needed [14]. However, even if the suitable combination can potentially lead to extremely efficient devices, some perovskite compositions, especially those used for wide-band gap absorbers, suffer from high-open-circuit voltage (V_{OC}) losses [13, 15]. For this issue, we have investigated the cross-linkable fullerene derivative [6,6]-phenyl-C61-butyl styryl dendron ester (c-PCBSD) in wide-band gap perovskite solar cells. This material was reported to have passivating properties, which led to decreased V_{OC} losses in organic photovoltaics. In addition, the device stability was increased [16]. In 2010, Hsieh et al. first synthesized this material and tested it as a cathodic buffer layer in organic solar cells [17]. They reported enhanced efficiency and device stability, suggesting c-PCBSD as a possible agent to prevent interfacial erosion, which can occur from multiple solvent treatments in complex many-layer devices like tandem solar cells. Li et al.

reported a passivation effect when implementing c-PCBSD into the perovskite absorber layer [18]. The efficiency and stability-improving impact of c-PCBSD in perovskite solar cells was reported in several cases [18–20]. No investigations of c-PCBSD in wide-band gap perovskite solar cells have been published to date. In this work, c-PCBSD was tested as an n-type interlayer in a p-i-n system between the wide-band gap perovskite ($\text{Cs}_{0.2}\text{FA}_{0.8}\text{Pb}(\text{I}_{0.5}\text{Br}_{0.5})_3$) and [6,6]-phenyl-C61-butyl styryl dendron ester (PC[60]BM). We have investigated the impact on the optoelectronic properties of the perovskite absorber and the device performance and stability.

Results and discussion

For the study of c-PCBSD as a cathodic interlayer in perovskite solar cells, devices according to the layer configuration shown in Fig. 1, with and without the addition of c-PCBSD, were fabricated. In both cases, with and without c-PCBSD, we were able to fabricate very well-performing wide-band gap solar cells with high fill factors of up to 77% and without indication of hysteresis during the current density–voltage measurements (j - V measurements) under 1 sun illumination (Fig. 2a). The concentration given in the graph refer to the PCBSD concentration in the anti-solvent chlorobenzene (CB) before cross-linking. We could obtain lower leakage currents from devices with c-PCBSD from the semi-logarithmic j - V curves in Fig. 2b, suggesting higher shunt resistance which is desirable in solar cells [21]. Figure 2c compares the external quantum efficiencies (EQE) of the two devices. The short-circuit current densities shown in the legend of this graph are calculated from the EQE spectra (Eq. (S10)). Due to the insulating properties of c-PCBSD [22], the current density in devices with cathodic interlayer was determined to

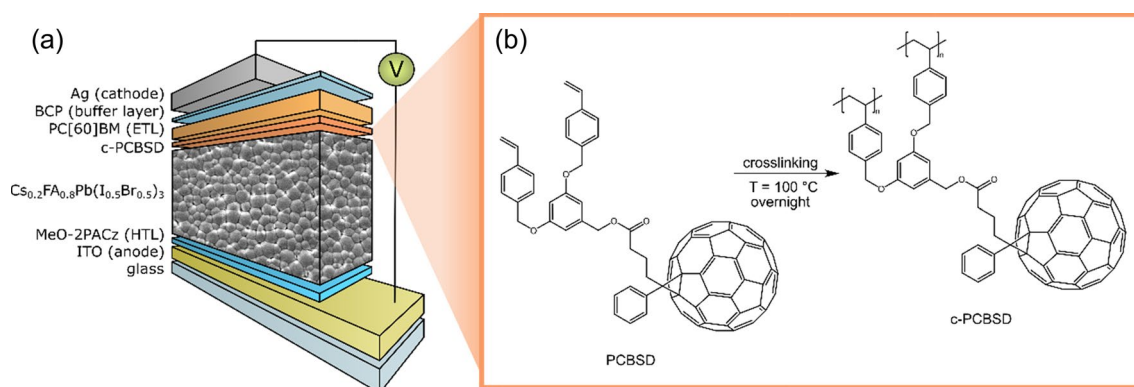


Fig. 1 Schematic illustration of a perovskite solar cell in p-i-n configuration in the following upward order: Anode/hole transport layer (HTL)/perovskite/ c-PCBSD (interlayer)/electron transport layer

(ETL)/buffer layer/cathode (a). Reaction equation for the cross-linking of PCBSD to form c-PCBSD (b)

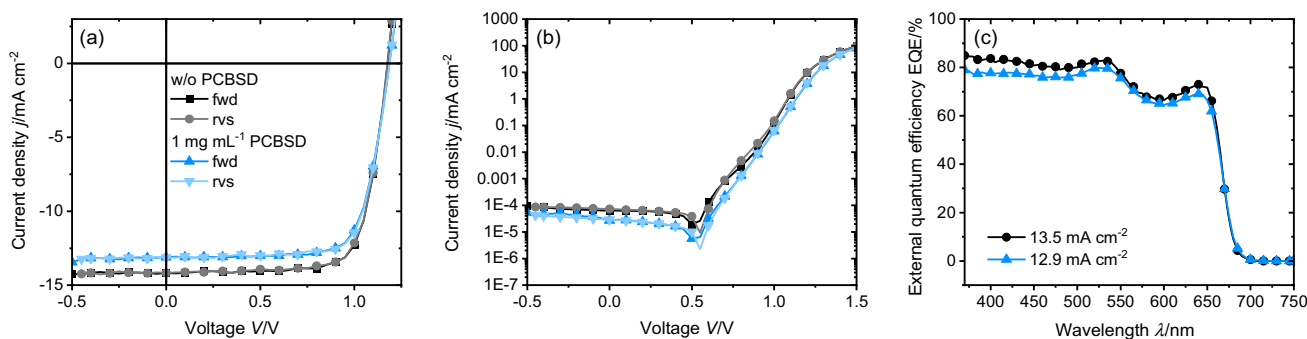


Fig. 2 Current density–voltage curves of perovskite solar cells, one without and one with 1 mg mL⁻¹ c-PCBSD layer, measured in forward (fwd) and reversed (rvs) direction: measured under 1 sun illumination

(a); measured in the dark (b). External quantum efficiency of solar cells and short-circuit current determined from these spectra (c)

be marginally lower compared to the pristine solar cells, which can be seen from the EQE measurements as well as from the j - V characteristics (Fig. 3 and Table S6). Figure 3 shows box plots of j - V parameters of solar cells with different concentrations of PCBSD. By incorporating c-PCBSD in the devices, the open-circuit voltage could be increased by 0.03 V for the best cell. On the contrary, the short-circuit current density was reduced. A lower open-circuit voltage was obtained for devices prepared with very low PCBSD concentrations in the antisolvent (0.25–0.5 mg mL⁻¹), compared to devices without PCBSD. We presume a shortage of cross-linkable material and, therefore, no dense film formation for PCBSD concentrations < 1 mg mL⁻¹. What can be clearly seen in Fig. 3b is a uniform decline of the short-circuit current density when increasing the amount of PCBSD. We were particularly interested in the origin of the enhanced open-circuit voltage of the modified devices since reduction of V_{OC} losses, especially in wide-band gap perovskite solar cells, is still a challenging and ongoing task [15]. Understanding the underlying physical principles at the

interface between the perovskite and c-PCBSD could give indications for the development of novel, more optimized interlayer materials. The absorbance of perovskite samples with and without c-PCBSD on top is shown in Fig. 4a. The optical band gap energies ϵ_g of these perovskite films were derived from a Tauc plot. The method is described in the supplementary information. All measured perovskite films with c-PCBSD (0.25–2 mg mL⁻¹) are determined to have a band gap of 1.85 eV. The band gap for a pristine perovskite film is 1.86 eV. For the calculation of the V_{OC} loss ($q \cdot \epsilon_g - V_{OC}$), the mean V_{OC} value was used.

For devices without and with 1 mg mL⁻¹ PCBSD, we could determine a V_{OC} loss of 0.69 V and 0.66 V, respectively, which are typical values for wide-band gap perovskite solar cells [13]. V_{OC}^{rad} refers to the open-circuit voltage when only radiative recombination occurs and is, therefore, higher than the measured V_{OC} [23]. V_{OC}^{rad} can be calculated with the classical diode equation by determining the photocurrent and the dark current with the solar spectrum AM1.5G and the black body radiation spectrum, respectively. The method is described in the following: V_{OC}^{rad} is

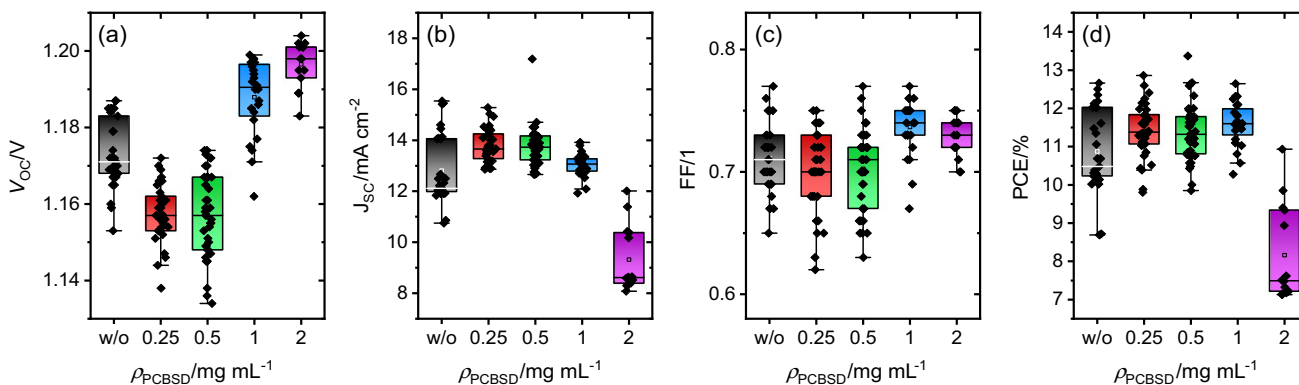


Fig. 3 Box plots of characteristic solar cell parameters extracted from current–voltage curves of cells with different PCBSD concentrations: **a** open-circuit voltage (V_{OC}), **b** short-circuit current (J_{SC}), **c** fill factor (FF), **d** power conversion efficiency (PCE)

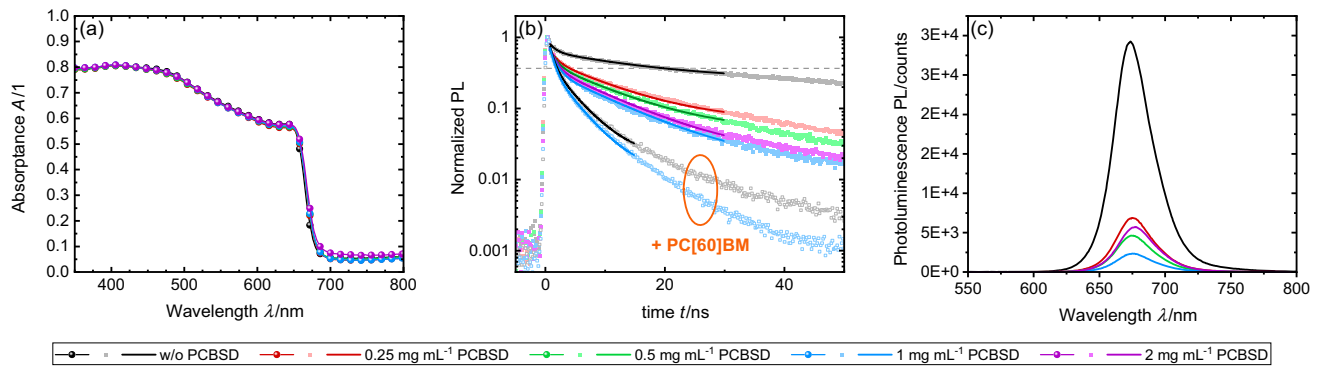


Fig. 4 Optical characterization of perovskite films on MeO-2PACz without and with different concentrations of PCBSD: absorbance (a); time-resolved photoluminescence (two additional films were measured with PC[60]BM on top) (b); steady-state photolumines-

cence of perovskite films (c). In panel (b), the solid lines represent the biexponential fitting curves of the decay graphs, while the dashed line indicates the value of $1/e$ of the normalized PL used for the determination of $\tau_{1/e}$

related to the open-circuit voltage (V_{OC}) via the electroluminescence quantum efficiency (ELQE) of the device (Eq. (S4)) [23]. If ELQE equals unity, then $V_{OC}^{rad} = V_{OC}$.

$$V_{OC}^{rad} = V_{OC} - \frac{kT}{q} \ln(\text{ELQE}). \quad (1)$$

V_{OC}^{rad} is calculated using Shockley's diode equation and assuming an ideality factor of 1 [24].

$$V_{OC}^{rad} = \frac{kT}{q} \ln\left(\frac{J_{PH}}{J_0} + 1\right). \quad (2)$$

J_{PH} refers to the photocurrent of the device, and J_0 to the current measured in the dark. Both can be determined using Eqs. (S6) and (S7), respectively.

$$J_{PH} = q \int_{\epsilon_g}^{\infty} \text{EQE}(E) \Phi_{SUN}(E) dE, \quad (3)$$

$$J_0 = q \int_{\epsilon_g}^{\infty} \text{EQE}(E) \Phi_{BB}(E) dE. \quad (4)$$

$\Phi_{SUN}(E)$ is the photon flux from the sun measured on earth (AM1.5G) and was downloaded from [25]. $\Phi_{BB}(E)$ is the black body radiation at 300 K, determined from Planck's law [26].

The difference between V_{OC}^{rad} and V_{OC} is the open-circuit voltage lost due to non-radiative recombination $\Delta V_{OC}^{non-rad}$. The values calculated for the voltage loss analysis are summarized in Table 1. With these calculations, we could determine a non-radiative voltage loss of 0.35 and 0.32 for solar cells without and with c-PCBSD, respectively. The V_{OC} loss caused by non-radiative recombination is, therefore, lower with c-PCBSD as interlayer. Suppression of non-radiative recombination is a prerequisite for the fabrication of efficient solar cells with high V_{OC} (compare with Eq. (S4)). To

Table 1 Voltage loss analysis of a solar cell with and without c-PCBSD, where ρ_{PCBSD} is the mass concentration of PCBSD in the anti-solvent, ϵ_g refers to the optical band gap determined from the absorption coefficient, $(q \cdot \epsilon_g - V_{OC})$ is the open-circuit voltage loss, V_{OC}^{rad} the open-circuit voltage if only radiative recombination occur and $\Delta V_{OC}^{non-rad}$ the open-circuit voltage loss due to non-radiative recombination

$\rho_{PCBSD}/\text{mg mL}^{-1}$	ϵ_g/eV	$(q \cdot \epsilon_g - V_{OC})/\text{V}$	V_{OC}^{rad}/V	$\Delta V_{OC}^{non-rad}/\text{V}$
w/o	1.86	0.69	1.52	0.35
1	1.85	0.66	1.51	0.32

investigate the impact of the addition of c-PCBSD on the charge carrier dynamics in the perovskite absorber layer, time-resolved photoluminescence measurements were performed by means of time-resolved single photon counting (TCSPC). The measurements were carried out on perovskite films on glass/ITO/MeO-2PACz without and with c-PCBSD deposited on the perovskite from solutions with concentrations of 0.25–2 mg mL⁻¹ PCBSD. For the same films without c-PCBSD and with the material deposited from a 1 mg mL⁻¹ solution, additional measurements were performed after deposition of the PC[60]BM electron transport layer. The normalized PL decay curves in Fig. 4b show a non-monoexponential behavior. Fitting of the curves was, thus, carried out with a biexponential function according to Eq. (1) in the range of the first several nanoseconds. The relevant processes occur within this time frame, as reflected by the decay of the vast majority of photoexcited states. For all transient PL curves, the transition into weak-intensity long-lived decay processes can be observed towards longer decay times. Due to their low contribution to the PL decay and, thus, negligible impact on the total excited state dynamics,

these longer decay components were not considered for the curve fitting.

$$y = y_0 + A_1 e^{-\frac{t}{\tau_1}} + A_2 e^{-\frac{t}{\tau_2}}. \quad (5)$$

From the time constants τ_1 and τ_2 determined from the fitting function, the average time constant τ_{avg} for the decay was calculated according to Eq. (2).

$$\tau_{\text{avg}} = \frac{A_1 \tau_1^2 + A_2 \tau_2^2}{A_1 \tau_1 + A_2 \tau_2}. \quad (6)$$

The results of the biexponential fitting of the PL decay curves are listed in Table 2. Comparison of the perovskite films with and without c-PCBSD shows a significant decrease in the decay time upon addition of a c-PCBSD layer. Results of the biexponential fitting show that the initial fast decay component has an almost identical time constant (τ_1) for the samples with and without c-PCBSD, while the time constant of the second decay component (τ_2) is considerably lower for the perovskite films with c-PCBSD. For the samples with c-PCBSD deposited from solutions of 0.25–2 mg mL⁻¹, the decay curves could be fitted well by functions with identical time constants τ_1 and τ_2 suggesting the same decay processes occurring in the samples. For increasing concentrations of PCBSD a larger contribution of the fast decay component (increasing A_1) and smaller contribution of the slower component (decreasing A_2) can be observed, resulting in a faster average decay. This trend peaks for a PCBSD concentration of 1 mg mL⁻¹, while for 2 mg mL⁻¹ the decay time slightly increases again. In accordance with the previous reports, the fast decay process (τ_1) can be attributed to a charge transfer process at the perovskite–hole/electron transport layer interface, while the slower component (τ_2) can be attributed to carrier recombination in the perovskite bulk [27, 28]. For the pristine perovskite films, the fast decay component can, thus, be ascribed to

a charge transfer to the MeO-PACz hole transport layer. The reduced decay time and larger contribution of the τ_1 decay process of the c-PCBSD modified films may consequently be attributed to an additional electron transfer from the perovskite layer to c-PCBSD. The charge carriers transferred to the respective charge transporting layers are not available for recombining with opposite charges in the perovskite bulk, which leads to quenching of the photoluminescence and a reduced time constant. Quenching of the perovskite PL for the films with c-PCBSD can be clearly observed from the steady-state PL spectra of the glass|ITO|MeO-2PACz|perovskite(lc-PCBSD) samples shown in Fig. 4c. For the films measured upon addition of the PC[60]BM electron transport layer on top of the perovskite or perovskite/c-PCBSD, respectively, a strongly accelerated PL decay can be observed in Fig. 4b. This can be attributed to an electron transfer to PC[60]BM. The decay curves with and without PCBSD indicate that the c-PCBSD interlayer facilitates the charge transfer, as shown by the decreased decay time. Improved charge extraction behavior probably originates from proper film formation of c-PCBSD on the perovskite, thus building up a good contact between perovskite and PC[60]BM. However, there is no enhanced electrical driving force since the LUMO of c-PCBSD is on the same level as the LUMO of PC[60]BM [17]. We propose that the improved charge extraction through c-PCBSD may reduce the non-radiative recombination via trap states and, thus, enable a decrease of the non-radiative V_{OC} loss in the solar cells.

In contrast to earlier reports [18–20], the lifetime of a device with c-PCBSD drastically decreased under continuous illumination. As measured by maximum power point tracking (Fig. S5), a solar cell with c-PCBSD reached 80% of the initial efficiency after 6 h. Contrarily, a pristine solar cell reached its t_{80} after 39 h. To the best of our knowledge, c-PCBSD was never used in combination with bromide salt-containing perovskites. We suppose chemical interaction with bromide and the cross-linkable additive might cause faster degradation of the solar cell. Additional

Table 2 Parameters obtained from biexponential fitting of time-correlated single photon counting measurements of perovskite films on glass|ITO|MeO-2PACz without and with different concentrations of PCBSD. A PC[60]BM layer was deposited on top of two additional films. τ_{avg} refers to the average time constant and $\tau_{1/e}$ is the time constant at $1/e$

$\rho_{\text{PCBSD}}/\text{mg mL}^{-1}$	A_1	τ_1/ns	A_2	τ_2/ns	y_0	$\tau_{\text{avg}}/\text{ns}$	$\tau_{1/e}/\text{ns}$	R^2
w/o	0.369	1.13	0.397	16.97	0.244	16.05	19.59	0.9954
0.25	0.391	1.12	0.431	10.42	0.065	9.59	4.04	0.9972
0.5	0.513	1.12	0.392	10.42	0.047	9.27	3.14	0.9985
1	0.687	1.12	0.335	10.42	0.016	8.73	2.70	0.9972
2	0.654	1.12	0.369	10.42	0.021	8.92	2.40	0.9977
w/o + PC[60]BM	0.939	0.81	0.438	4.15	0.020	3.17	2.00	0.9992
1 + PC[60]BM	0.985	0.81	0.392	4.05	0.012	2.97	1.81	0.9996

experiments to gain a better understanding of the degradation mechanism are subject of further studies.

Conclusion

In this work, we fabricated wide-band gap perovskite solar cells without and with *c*-PCBSD as cathodic interlayer. The devices with the additional interlayer showed an improved open-circuit voltage as compared to pristine devices. Voltage loss analysis suggests a decreased non-radiative V_{OC} loss for cells with *c*-PCBSD. Spectroscopic measurements were conducted to study the origin of the lower V_{OC} loss. There is clear evidence of faster electron transfer in perovskite films modified with *c*-PCBSD as shown by transient and steady-state photoluminescence spectroscopy. The lower short-circuit current density obtained from solar cells with *c*-PCBSD is considered to occur due to the low charge carrier mobility of this material. A major drawback of the interlayer is the significantly reduced device stability of the wide-band gap perovskite solar cell. Due to promising results for V_{OC} improvement and encouraging works reported in the past, the application of *c*-PCBSD in perovskite solar cells deserves further investigation. A fundamental understanding of the interaction between the cross-linkable fullerene derivative and the bromide-containing perovskite layer is required to build a bridge between performance improvement and device's lifetime.

Experimental

Perovskite thin film and solar cell fabrication

Substrate preparation

Glass/ITO slices were patterned by partially covering them with PVC tape (1.5 cm of the 2.5 cm broad slice) and etching them in concentrated hydrochloric acid. After rinsing with water, the PVC tape was removed, and the slices were cut into pieces of 2.5×2.5 cm². The final glass/ITO substrate pattern is shown in Fig. S2 (a). After patterning, the substrates were cleaned by sequential ultrasonication in a 2% (v/v) aqueous solution of Hellmanex II (Hellma), deionized water, acetone and isopropanol, respectively.

Solution preparation

The following solutions were prepared one day before starting with spin-coating deposition and stirred at room temperature overnight: 0.3 mg mL⁻¹

[2-(3,6-dimethoxy-9*H*-carbazol-9-yl)ethyl]phosphonic acid (MeO-2PACz) in anhydrous ethanol; 1.08 M perovskite precursor solution (details below); 100 mg mL⁻¹ thiourea in dimethylformamide (DMF); 0.25–2 mg mL⁻¹ PCBSD in chlorobenzene (CB); 20 mg mL⁻¹ PC[60]BM in chloroform/CB = 3:1; 0.5 mg mL⁻¹ 2,9-dimethyl-4,7-diphenyl-1,10-phenanthroline (BCP) in anhydrous ethanol. For 1 mL of a 1.08 M perovskite precursor solution, 345.76 mg lead iodide, 91.75 mg lead bromide, 42.56 mg cesium bromide, and 99.98 mg formamidinium bromide were dissolved in a mixture of DMF/*N*-methyl-2-pyrrolidinone (NMP) = 70:30 (v/v). Before use, the precursor solution was filtered (45 μm PTFE filter, Fisher Scientific); then, 10 μL of the thiourea solution was added to 1 mL of the filtered precursor solution.

Spin coating

All spin-coating steps were performed under a nitrogen glove box atmosphere ($H_2O < 0.1$ ppm; $O_2 < 10$ ppm). Before spin coating, the substrates were treated with oxygen plasma (100 W, 10 min). The solar cells were fabricated in a p-i-n configuration in the sequence glass/ITO/MeO-2PACz/Perovskite(*c*-PCBSD)/PC[60]BM/BCP/Ag. For the first layer, MeO-2PACz, the spin speed was 3000 rpm for 30 min (1500 rpm s⁻¹), followed by annealing at 100 °C for 10 min. Patterning of substrate edges (see Fig. S2(b)) was always done after 5 min of annealing (if annealing was required) by using a cotton bud and 40 μL of the same solvent as it was used for dissolving the respective material. MeO-2PACz was wetted during spinning with 200 μL methanol (210 μL s⁻¹) at a spin speed of 4000 rpm to achieve a monolayer. The substrate spun for another 20 s. Right after the end of the spin program, 200 μL perovskite precursor solution was applied to the substrate. After approximately 10 s, the spin-coating program was initiated (480 rpm for 8 s with 480 rpm s⁻¹, then 4000 rpm for 58 s with 2000 rpm s⁻¹) followed by dropping 200 μL of the anti-solvent at 40 to 38 s before the end of the spinning program. Either CB or a solution of PCBSD in CB was used as an anti-solvent. Immediately after spinning, the substrate was annealed at 65 °C for 2 min, followed by annealing at 100 °C overnight. Extensive heat treatment is required to initiate cross-linking of PCBSD to form *c*-PCBSD [18]. For perovskite films without PCBSD, 10 min of annealing is sufficient. In this work, all solar cells were treated the same; therefore, all cells were annealed overnight after perovskite (and PCBSD) deposition. PC[60]BM was spin-coated at 1320 rpm for 16 s (660 rpm s⁻¹), followed by 1980 rpm for 15 s (990 rpm s⁻¹). BCP was deposited at a spin speed of 4000 rpm for 30 s, with an acceleration of 2000 rpm s⁻¹. For PC[60]BM and BCP, no annealing is required.

Top contact evaporation and encapsulation

100 nm top contacts (Ag) were evaporated in UNIVEX thermal evaporator (Leybold). The solar cells were encapsulated using E131 epoxy resin for EQE measurements, photoluminescence, and MPP tracking.

Absorptance, absorption coefficient, and band gap determination

Transmittance and reflectance spectra of glass|ITO|MeO-2PACz|Perovskite|(c-PCBSD) samples were recorded with a double-beam spectrometer (Perkin Elmer UV–Vis–NIR Lambda 1050) equipped with a 150 mm integrating sphere. For the reflectance R , a silicon wafer sample was used as a reference. Absorptance A was determined from transmittance T and reflectance R using Eq. (S8). For calculating the absorption coefficient α , Eq. (S9) was used. The layer thicknesses were determined with a Dektak profilometer. The optical band gaps of the perovskite films were determined from a Tauc plot (for the method, see supplementary information).

Current–voltage measurements

I – V characteristics were measured using a source measure unit (Keithley Source Meter 2401) in a voltage range from -0.5 – 1 V (forward bias) and reversed with voltage steps of 0.05 V, under 1 ± 0.02 sun(s) illumination (AM1.5G, LOT-Quantum Design Xenon arc lamp, Mencke & Tegtmeier GmbH silicon solar cell for calibration). The pixel area was estimated with a caliper.

External quantum efficiency

The external quantum efficiency of the fabricated solar cells was measured using a potentiostat (Jaisle, Model 1002 T-NC) and a lock-in amplifier (173 Hz, Stanford Research Systems, Model SR 830 DSP). The sample was illuminated with monochromatic light from an Oriel Instruments monochromator with a xenon arc lamp (LOT-Quantum Design) as the source. Light intensity was calibrated with a silicon photodiode (Hamamatsu S2281).

Photoluminescence

Glass|ITO|MeO-2PACz|Perovskite|(c-PCBSD) samples (c-PCBSD is optional) were illuminated from the glass

side using a Coherent Obis LX 405 nm laser, powered with 3.48 mW. The sample emission is directed with a glass fiber over two LP 420 optical filters to the CCD sensor (Andor CD420A-OE). The shown photoluminescence spectra are background corrected.

Time-resolved photoluminescence

Time-correlated single photon counting (TCSPC) measurements were performed on a setup consisting of a Becker & Hickl SPC 150 TCSPC module and a PMC-100-1 photomultiplier. For emission wavelength selection, a DeltaNu DNS-300 monochromator (slit widths: 3 mm) was used. Pulsed excitation light was provided by an NKT Photonics SuperK FIANIUM FIU-15 supercontinuum white light laser equipped with a pulse picker and a fiber-coupled Photon Etc LLTF Contrast VIS unit for wavelength selection. For all measurements, an excitation wavelength of 480 nm was used. The emission was detected at the emission maximum of the respective samples as determined by steady-state PL measurements. The full-width at half-maximum (FWHM) of the instrument response function of the used TCSPC setup is 0.22 ns. PL decay curves were fitted with a biexponential function, shown in Eq. (1). Average decay time constants were calculated according to Eq. (2). The fitting range for Glass|ITO|MeO-2PACz|Perovskite|(c-PCBSD) films was 0–30 ns and for films with an additional PC[60]BM layer on top 0–15 ns.

Supplementary Information The online version contains supplementary material available at <https://doi.org/10.1007/s00706-023-03103-1>.

Acknowledgements The authors acknowledge the funding from FFG in the frame of project no. 865072 and no. FP999888408. We acknowledge WTZ for financial support within project no. TW04/2021 to Prof. Niyazi Serdar Sariciftci.

Funding Open access funding provided by Johannes Kepler University Linz.

Data availability The data supporting this study's findings are available from the corresponding author upon reasonable request.

Open Access This article is licensed under a Creative Commons Attribution 4.0 International License, which permits use, sharing, adaptation, distribution and reproduction in any medium or format, as long as you give appropriate credit to the original author(s) and the source, provide a link to the Creative Commons licence, and indicate if changes were made. The images or other third party material in this article are included in the article's Creative Commons licence, unless indicated otherwise in a credit line to the material. If material is not included in the article's Creative Commons licence and your intended use is not permitted by statutory regulation or exceeds the permitted use, you will need to obtain permission directly from the copyright holder. To view a copy of this licence, visit <http://creativecommons.org/licenses/by/4.0/>.

References

- Chen Y, Zhang L, Zhang Y, Gao H, Yan H (2018) *RSC Adv* 8:10489
- deQuilettes DW, Zhang W, Burlakov VM, Graham DJ, Leijtens T, Osherov A, Bulović V, Snaith HJ, Ginger DS, Stranks SD (2016) *Nat Commun* 7:11683
- Lim J, Hörantner MT, Sakai N, Ball JM, Mahesh S, Noel NK, Lin Y-H, Patel JB, McMeekin DP, Johnston MB, Wenger B, Snaith HJ (2019) *Energy Environ Sci* 12:169
- Braly IL, deQuilettes DW, Pazos-Outón LM, Burke S, Ziffer ME, Ginger DS, Hillhouse HW (2018) *Nature Photon* 12:355
- Kojima A, Teshima K, Shirai Y, Miyasaka T (2009) *J Am Chem Soc* 131:6050
- Best Research-Cell Efficiency Chart (2022) National Renewable Energy Laboratory. <https://www.nrel.gov/pv/cell-efficiency.html>. Accessed 22 Dec 2022
- Shockley W, Queisser HJ (1961) *J Appl Phys* 32:510
- Sutter-Fella CM, Li Y, Amani M, Ager JW, Toma FM, Yablono-vitch E, Sharp ID, Javey A (2016) *Nano Lett* 16:800
- Würfel P, Würfel U (2016) *Physics of solar cells*. Wiley-VCH, Weinheim
- Kim D, Jung HJ, Park IJ, Larson BW, Dunfield SP, Xiao C, Kim J, Tong J, Boonmongkolras P, Ji SG, Zhang F, Pae SR, Kim M, Kang SB, Dravid V, Berry JJ, Kim JY, Zhu K, Kim DH, Shin B (2020) *Science* 368:155
- Tandem solar cell achieves 32.5 percent efficiency (2022) *Science News in Science Daily*. <https://www.sciencedaily.com/releases/2022/12/221219164845.htm>. Accessed 27 Dec 2022
- Xie B, Chen Z, Ying L, Huang F, Cao Y (2020) *InfoMat* 2:57
- Brinkmann KO, Becker T, Zimmermann F, Kreusel C, Gahlmann T, Theisen M, Haeger T, Olthof S, Tüchtmantel C, Günster M, Maschwitz T, Göbelsmann F, Koch C, Hertel D, Caprioglio P, Peña-Camargo F, Perdígón-Toro L, Al-Ashouri A, Merten L, Hinderhofer A, Gomell L, Zhang S, Schreiber F, Albrecht S, Meerholz K, Neher D, Stollerfoht M, Riedl T (2022) *Nature* 604:280
- Wang J, Xie S, Zhang D, Wang R, Zheng Z, Zhou H, Zhang Y (2018) *J Mater Chem A* 6:19934
- Rajagopal A, Stoddard RJ, Jo SB, Hillhouse HW, Jen AK-Y (2018) *Nano Lett* 18:3985
- Voroshazi E, Cardinaletti I, Conard T, Rand BP (2014) *Adv Energy Mater* 4:1400848
- Hsieh C-H, Cheng Y-J, Li P-J, Chen C-H, Dubosc M, Liang R-M, Hsu C-S (2010) *J Am Chem Soc* 132:4887
- Li M, Chao Y-H, Kang T, Wang Z-K, Yang Y-G, Feng S-L, Hu Y, Gao X-Y, Liao L-S, Hsu C-S (2016) *J Mater Chem A* 4:15088
- Li M, Wang Z-K, Kang T, Yang Y, Gao X, Hsu C-S, Li Y, Liao L-S (2018) *Nano Energy* 43:47
- Chao Y-H, Huang Y-Y, Chang J-Y, Peng S-H, Tu W-Y, Cheng Y-J, Hou J, Hsu C-S (2015) *J Mater Chem A* 3:20382
- Coutts TJ (1978) *Thin Solid Films* 50:99
- Cheng Y-J, Hsieh C-H, Li P-J, Hsu C-S (2011) *Adv Funct Mater* 21:1723
- Rau U (2007) *Phys Rev B* 76
- Shockley W (1949) *Bell Syst Tech J* 28:435
- Standard Solar Spectra ASTM G-173-03 (2022) Photovoltaic Education. <https://www.pveducation.org/pvcdrom/appendices/standard-solar-spectra>. Accessed 30 Dec 2022
- Planck M (1900) *Verhandlungen der Deutschen Physikalischen Gesellschaft* 202
- Jiang T, Chen Z, Chen X, Chen X, Xu X, Liu T, Bai L, Yang D, Di D, Sha WEI, Zhu H, Yang YM (2019) *ACS Energy Lett* 4:1784
- Baloch AAB, Alharbi FH, Grancini G, Hossain MI, Nazeeruddin MK, Tabet N (2018) *J Phys Chem C* 122:26805

Publisher's Note Springer Nature remains neutral with regard to jurisdictional claims in published maps and institutional affiliations.